North Atlantic Extratropical Rossby Wave Breaking during the Warm Season: Wave Life Cycle and Role of Diabatic Heating

GAN ZHANG AND ZHUO WANG

Department of Atmospheric Sciences, University of Illinois at Urbana–Champaign, Urbana, Illinois

(Manuscript received 15 July 2017, in final form 8 January 2018)

ABSTRACT

This study investigates the life cycle of anticyclonic Rossby wave breaking during the extended warm season (July–October) over the North Atlantic basin. It was found that upper-tropospheric breaking waves are coupled with lower-level perturbations and can be traced back to a wave train that extends from the North Pacific. The overturning of potential vorticity (PV) contours during wave breaking is associated with the rapid development of an upper-level ridge, which occurs along the east coast of North America and over a warm and moist airstream. The ridge development is investigated using the PV budget analysis and trajectory analysis. The PV budget analysis suggests that the horizontal advection of PV by the perturbed flow dictates the movement and the later decay of the ridge. The ridge amplification, opposed by the horizontal advection of PV, is driven by the vertical advection and the diabatic production of PV, both of which are connected to diabatic heating. The vital role of diabatic heating in the ridge amplification is corroborated by the trajectory analysis. The analysis suggests that diabatic heating reduces the static stability near the tropopause and contributes to the ridge-related negative PV anomalies. The role of diabatic heating in anticyclonic and cyclonic wave breaking in other regions is also discussed. The findings suggest that moist diabatic processes, which were often excluded from the earlier studies of wave breaking, are crucial for Rossby wave breaking during the warm season. The updated understanding of wave breaking may benefit weather forecasting and climate predictions.

1. Introduction

Rossby waves play important roles in weather and climate variability. When Rossby waves attain large amplitudes or propagate into regions where the mean flow is comparable to the wave phase speed (Vallis 2017), the waves often deform rapidly and irreversibly because of nonlinear dynamical effects (McIntyre and Palmer 1983; Randel and Held 1991). The nonlinear deformation of Rossby waves (e.g., Haynes and McIntyre 1987a), known as wave breaking, occurs frequently throughout all seasons (Postel and Hitchman 1999; Abatzoglou and Magnusdottir 2006) and often coincides with the final stage in the life cycle of extratropical baroclinic waves (e.g., Thorncroft et al. 1993).

Rossby wave breaking is not only associated with momentum transport (e.g., Randel and Held 1991) and material transport (e.g., Appenzeller and Davies 1992; Waugh and Polvani 2000), but also modulates jet streams and some climate modes (e.g., Franzke et al. 2004; Rivière and Orlanski 2007; Woollings et al. 2008; Strong and Magnusdottir 2008). Recently the relation between wave breaking and high-impact weather events has been a subject of intense research. Mounting evidence suggests that wave breaking can be associated with atmospheric blocking (e.g., Tyrlis and Hoskins 2008; Masato et al. 2013), atmospheric rivers (e.g., Ryoo et al. 2013; Payne and Magnusdottir 2014), and other weather features that may contribute to heavy precipitation (e.g., Knippertz and Martin 2005; Martius et al. 2006, 2013) or extreme temperature (e.g., Sprenger et al. 2013; Parker et al. 2014). Beyond affecting the midlatitudes, wave breaking can also promote extreme moisture transport into the Arctic (Liu and Barnes 2015) and affect tropical convective activity (e.g., Kiladis 1998; Funatsu and Waugh 2008). Therefore, wave breaking is also a crucial process for the interaction between the midlatitudes and other latitudes.

In the context of tropical–extratropical interactions, the relation between extratropical breaking waves and tropical cyclones has motivated many recent studies. While the extratropical transition of recurving tropical

Corresponding author: Gan Zhang, gzhang13@illinois.edu

DOI: 10.1175/MWR-D-17-0204.1

cyclones can modify the midlatitude flow and lead to wave breaking downstream (e.g., Riemer and Jones 2014; Archambault et al. 2015; Grams and Archambault 2016), breaking extratropical waves can also extend into to the low latitudes and affect the development of tropical cyclones. Although the breaking waves can occasionally trigger tropical and subtropical cyclogenesis (e.g., Davis and Bosart 2004; Galarneau et al. 2015; Bentley et al. 2016, 2017), an overall negative correlation holds between Rossby wave breaking and Atlantic tropical cyclone activity on the seasonal time scale (Zhang et al. 2016, 2017). How tropical cyclones and extratropical waves interact with each other are highly sensitive to their phase relationship and the flow configuration, as suggested by modeling studies (Riemer and Jones 2014; Leroux et al. 2016) and observational analyses (Hanley et al. 2001; Galarneau et al. 2015; Zhang et al. 2017). The sensitivity poses a challenge for weather forecasting (e.g., Fitzpatrick et al. 1995; Davis and Bosart 2004) and the subseasonal-to-seasonal prediction.

Despite the large body of studies pertaining to wave breaking, the life cycle of breaking waves during the warm season has received limited attention. From an observational standpoint, the preceding studies suggested the mutual influences of tropical cyclones and warm-season breaking waves (e.g., Archambault et al. 2015; Galarneau et al. 2015; Zhang et al. 2016, 2017), but the life cycle of breaking waves during the warm season has not been well studied. From a theoretical standpoint, the existing understanding of the life cycle of breaking waves is mainly based on dry simulations of waves in strong baroclinic environments (e.g., Thorncroft et al. 1993; Peters and Waugh 1996; Polvani and Esler 2007). These dry simulations capture many fundamental aspects of wave development and afford valuable insights into the wave–flow interaction involved in wave breaking. However, their idealized model configuration differs from the warm-season midlatitude environment in the real atmosphere, which is usually less baroclinic. In addition, the environmental moisture and the associated diabatic processes can modulate the evolution of baroclinic waves (e.g., Whitaker and Davis 1994; Parker and Thorpe 1995; Moore and Montgomery 2004; Boettcher and Wernli 2011; Chagnon et al. 2013; Tamarin and Kaspi 2016). There is also evidence suggesting that including moisture, even in a strongly baroclinic environment, affects the behavior of breaking waves in idealized (Orlanski 2003) and real (e.g., Posselt and Martin 2004) simulations. More specifically, some case studies of the warm-season heavy precipitation (Massacand et al. 2001) and recurving tropical cyclones (Grams and Archambault 2016) showed that the release of latent heat in an amplifying upstream ridge facilitates the downstream wave breaking. The co-occurrences of breaking waves and strong moist airstreams that ascend in extratropical cyclones, namely warm conveyor belts, were examined in Madonna et al. (2014). However, it is surprising that the study found only 10 co-occurrences over the North Atlantic during June–November of 1989–2009 (their Table 1). The rarity appears to contradict our empirical knowledge from case analyses, which suggests that diabatic heating is regularly involved in wave breaking. We note that the warm conveyor belts considered by Madonna et al. (2014) include only events with intense ascending from the lowermost troposphere; it is possible that moderate diabatic heating and ascending motion contribute to wave breaking regularly.

A key step toward better understanding and predicting breaking waves during the warm season is to characterize their life cycle in a realistic environment. In this study, we will use observation-constrained reanalysis data to analyze the composites of more than 400 breaking waves during July–October. The study will 1) examine the life cycle of breaking waves during the warm season, and 2) explore how diabatic processes affect the life cycle of those breaking waves. The findings will be discussed in the context of both theoretical research and weather forecasting. The rest of the paper is organized as follows: section 2 provides an overview of data and methodology used in the study. Section 3 describes the life cycle of breaking waves and their connection with upstream and downstream weather perturbations. Section 4 investigates the roles of diabatic processes in producing a key feature of breaking waves. The concluding section summarizes and discusses the findings.

2. Data and methodology

a. Reanalysis data

The study uses the 6-hourly data from the ERA-Interim (Dee et al. 2011). The data are coarsened to a 2.5° horizontal grid to facilitate its storage and processing. We primarily use the data on the isobaric levels because the high vertical resolution is helpful for conducting the vertical differentiation and examining the wave structure. In addition to the isobaric data, the data on the 350-K isentropic surface is used to identify wave breaking near the tropopause.

b. Identification of breaking waves

We use the algorithm described in Strong and Magnusdottir (2008) to identify extratropical wave breaking by searching for the overturning of PV contours. More specifically, the algorithm examines circumglobal PV contours and reports the features that

make a specific PV contour cross a particular meridian more than once. Following Zhang et al. (2016, 2017), we search the PV contours that range from 1.5 to 7.0 PV units (PVU; 1 PVU = 10^{-6} K kg^{-1} m^2 s^{-1}) at 0.5-PVU intervals. The search is conducted on the 350-K isentropic surface, which is close to the 200-hPa surface and near the level of the upper-tropospheric jet. Notably, wave breaking occurs most often near this level during the warm season (Abatzoglou and Magnusdottir 2006; Hitchman and Huesmann 2007). The overturning of PV contours is associated with equatorward intrusions of high-PV air, namely high-PV tongues (Fig. 1a). For a breaking wave at a specific location, the overturning may be present on several PV contours between 1.5 and 7.0 PVU, and the algorithm retains the most extensive high-PV tongue (Strong and Magnusdottir 2008). We locate the centroid and calculate the area of the high-PV tongue and record the information for the postprocessing. To ensure consistency with the companion studies (Zhang et al. 2016, 2017), we examine the breaking waves over the subtropical North Atlantic (Fig. 1b) during July–October of 1979–2013. The domain of interest is approximately 20°–35°N, 45°–85°W and corresponds to the western subdomain in Zhang et al. (2017), where breaking waves strongly affect tropical cyclone activity. The settings emphasize anticyclonic wave breaking (Thorncroft et al. 1993; Peters and Waugh 1996), which is characterized by the anticyclonic rotation of low-PV and high-PV air. During the period of interest, anticyclonic wave breaking accounts for about 75% of wave breaking events over the entire North Atlantic basin and nearly all the events on the equatorward flank of the midlatitude jet.

In many cases, the overturning of PV contours at adjacent time steps in our domain of interest is related to the same baroclinic wave. These time steps correspond to various stages of the wave life cycle (see section 3a). If all those time steps were used as the reference time to build lead–lag composites, the ambiguity of temporal phasing would contaminate the composite sequence of the wave life cycle. To address this issue, we select the life stage when the extent of equatorward high-PV intrusions maximizes as the reference time. More specifically, we calculate the area of the equatorward intrusions associated with breaking waves on the 6-hourly basis. For the 6-hourly series in each year, the area anomalies associated with the intrusions are calculated by removing the climatological seasonal cycle and the seasonal means of individual years. We next search for the local maxima that 1) deviate from zero by at least one standard deviation and 2) are the largest within a time window of ±2.5 days. The time steps that meet these conditions are defined as the reference time ($T = 0$ h). Each of these reference time steps ($N = 429$) is considered to correspond to an individual breaking wave. Based on the reference time, we use both case analysis and lead–lag composites to illustrate the wave life cycle. Although the criteria in selecting reference time are somewhat subjective, the output reasonably agrees with manual analyses. Varying the settings, such as using thresholds of 0.5 to 1.5 standard deviations or time windows of ±2 to ±4 days, affects the sample size of breaking waves (Table 1) but does not affect their qualitative characteristics.

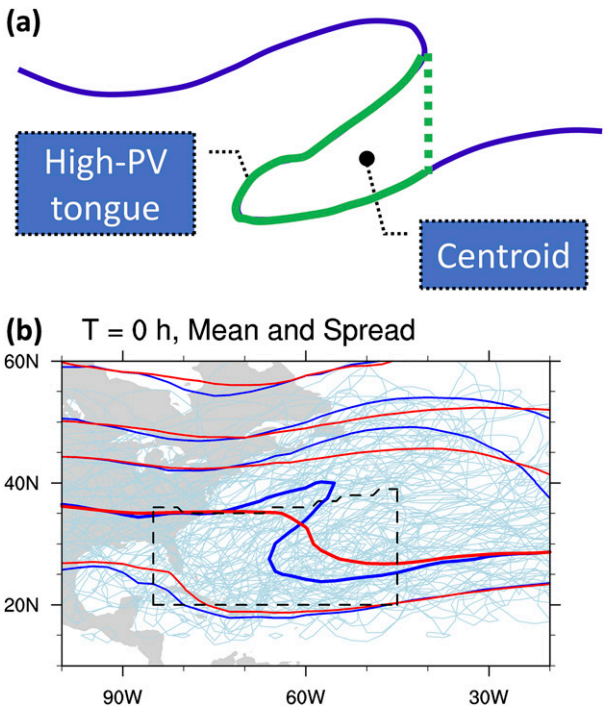

FIG. 1. (a) A schematic of overturning PV contour related to anticyclonic Rossby wave breaking. The blue line stands for a PV contour, green line highlights the high-PV tongue associated with wave breaking, and the black dot denotes the centroid of high-PV tongue. The high-PV tongue is enclosed by a PV contour (green solid line) and a meridian (green dashed line) determined by the north inflection point of the PV contour. (b) The 350-K PV distribution of climatology mean (red contours) during July–October of 1981–2010 and composite of breaking waves (blue contours; $N = 429$) at the reference time ($T = 0$ h). From south to north, the PV values are contoured at 1, 2, 4, 6, and 8 PVU. The breaking waves used in the composite analyses have their centroids of high-PV tongues located in the western subdomain in Zhang et al. (2017). The northern boundary of the domain is 10°S of the axis of the 200-hPa climatological jet. The domain is highlighted by the black dashed lines. In addition, we randomly selected 40 breaking waves and plotted their 2-PVU contours using light blue lines.

c. *Analyses of PV tendency*

When examining how physical processes contribute to wave breaking, we use the PV framework as it intuitively unifies dynamic and thermodynamic perspectives. The

TABLE 1. Sensitivity test for the selection of breaking waves (see section 2b). Criterion 1: the deviation threshold (Dev) ranges from 0.50 to 1.50 standard deviations of the area index. Criterion 2: the time window (T_win) ranges from 2.0 to 4.0 days.

	Dev = 0.50	Dev = 0.75	Dev = 1.00	Dev = 1.25	Dev = 1.50
T_win = 2.0 day	605	546	475	427	380
T_win = 2.5 day	526	485	429	389	346
T_win = 3.0 day	466	439	397	360	319
T_win = 3.5 day	430	409	372	339	300
T_win = 4.0 day	391	371	339	313	285

tendency of PV can be linked to diabatic processes using the following approximation (e.g., Haynes and McIntyre 1987b; Posselt and Martin 2004):

$$\frac{dq}{dt} = -g\boldsymbol{\eta}_a \cdot \nabla\left(\frac{d\theta}{dt}\right), \tag{1}$$

where q is the isobaric PV, t is the time, d/dt is the material derivative, g is the gravitational acceleration, $\boldsymbol{\eta}_a$ is the 3D absolute vorticity, ∇ is the 3D gradient operator in the isobaric coordinates, and θ is the potential temperature. Our analyses use a rearranged form of this equation to evaluate the local change rate of PV:

$$\frac{\partial q}{\partial t} = -\mathbf{V} \cdot \nabla q - g\boldsymbol{\eta}_a \cdot \nabla\left(\frac{d\theta}{dt}\right), \tag{2}$$

where $\partial/\partial t$ the local change rate, and $\mathbf{V}$ is the wind vector. The first term of the right-hand side represents the 3D advection of PV, and the second term represents the diabatic production of PV. We will expand these two terms to analyze how various processes contribute to the PV anomalies during wave breaking, as will be further discussed in section 4.

d. Diabatic heating and data assimilation

To calculate the diabatic production of PV, one needs the information of diabatic heating ($d\theta/dt$). In the reanalysis system, the potential temperature field is modified by the physical processes described by the thermodynamics equations and the process of data assimilation (Fueglistaler et al. 2009). The potential temperature tendency thus can be expressed in the following form:

$$T_{\text{local}} + T_{\text{adv}} = T_{\text{physics}} + T_{\text{assim}}, \tag{3}$$

where T_{local} is the local tendency, T_{adv} is the tendency contributed by the 3D advection, T_{physics} is the tendency forecasted by the parameterized model physics, and T_{assim} is the tendency introduced by the data assimilation. The left-hand side of Eq. (3) can be written as

$$T_{\text{local}} + T_{\text{adv}} = \frac{\partial\theta}{\partial t} + \mathbf{V} \cdot \nabla\theta = \frac{d\theta}{dt}. \tag{4}$$

The expression is often used to estimate T_{physics} (e.g., Ling and Zhang 2013; Tamarin and Kaspi 2016), which is related to physical processes including radiation, cloud microphysics, turbulent mixing, etc. However, such an estimate of T_{physics} is only accurate when T_{assim} is small or zero. Alternatively, T_{physics} can be acquired from the direct model output. In the case of ERA-Interim, T_{physics} is provided at 3-h intervals in the form of temperature tendency accumulated during 12-h model forecasts (Berrisford et al. 2011). Using the data, we calculate the 6-hourly accumulation of T_{physics} and consider its difference from the left-hand side of Eq. (3) as T_{assim}. Assuming that the errors in calculating the left-hand side of Eq. (3) are small—but not necessarily negligible (see section 4a)—large values of T_{assim} would suggest that the data assimilation strongly constrain the tendency of potential temperature, implying that the parameterized model physics may have trouble in producing the observed changes. We will examine T_{physics} and T_{assim} to infer the performance of parameterized model physics in capturing the temperature tendencies related to breaking waves.

e. Trajectory analysis

To investigate the accumulated impacts of diabatic heating, we also carried out trajectory analysis using the Lagrangian Analysis Tool (LAGRANTO, version 2; Sprenger and Wernli 2015). This tool can locate the air parcels of interest within a specified time range and output the properties of air parcels along their trajectories. Although the coarse spatial and temporal resolution of the reanalysis data may limit the accuracy of the trajectory analysis, the analysis complements the PV budget analyses and is useful in diagnosing diabatic heating during the wave life cycle.

3. Life cycle of breaking waves

a. Overview of Rossby wave breaking

For the convenience of discussion, we start with an overview of breaking waves ($N = 429$) at the reference time ($T = 0$ h). Consistent with the broad domain where the breaking waves were identified, Fig. 1b shows that

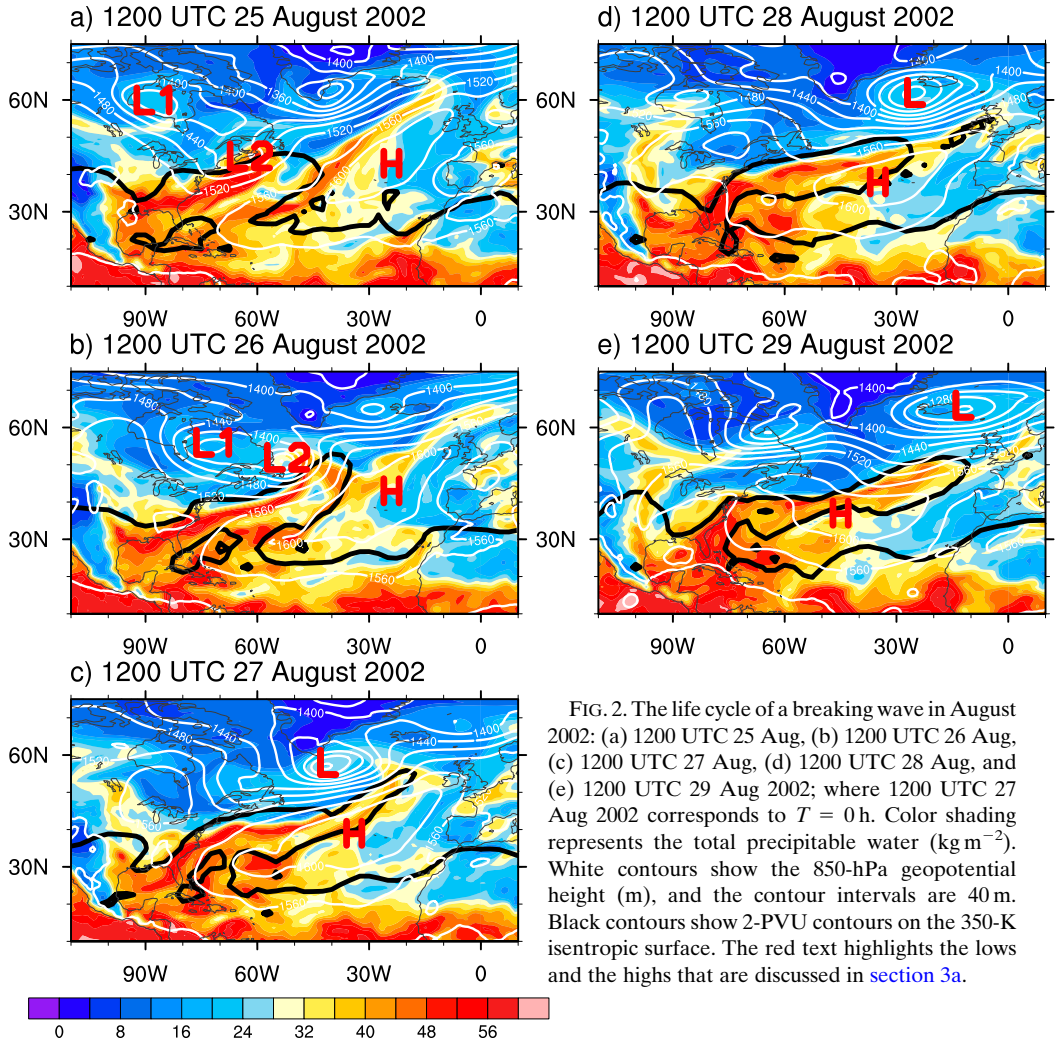

FIG. 2. The life cycle of a breaking wave in August 2002: (a) 1200 UTC 25 Aug, (b) 1200 UTC 26 Aug, (c) 1200 UTC 27 Aug, (d) 1200 UTC 28 Aug, and (e) 1200 UTC 29 Aug 2002; where 1200 UTC 27 Aug 2002 corresponds to $T = 0$ h. Color shading represents the total precipitable water (kg m^{-2}). White contours show the 850-hPa geopotential height (m), and the contour intervals are 40 m. Black contours show 2-PVU contours on the 350-K isentropic surface. The red text highlights the lows and the highs that are discussed in section 3a.

the 2-PVU contours of individual breaking waves have large variability. In many cases, the perturbed flow involved in wave breaking causes the 2-PVU contour to deviate far away from the climatological mean position. The deviation is also clear in the composite of breaking waves, which shows that the composite mean 2-PVU contour overturns over the western Atlantic (near 30°N, 60°W), featuring high-PV air that wraps anticyclonically around an area of relatively low PV. The equatorward intrusion of high-PV air, as emphasized in Zhang et al. (2016, 2017), results in significant extratropical impacts on tropical atmosphere. To the northeast of the high-PV air, the PV contours displace northward from their climatological positions, and the displacement is accompanied by the southward displacement of PV contours both upstream and downstream.

Many environmental variations accompany wave breaking. Here we briefly discuss some variations associated with the life cycle of a breaking wave in August 2002 (Fig. 2). The case is selected because of its extensive high-PV tongue and well-defined meteorological features. As one of the 429 identified breaking waves, this case has signatures of wave breaking at a few consecutive time steps. At 1200 UTC 27 August 2002, the high-PV tongue is the most extensive, so the time step corresponds to the reference time ($T = 0$ h) (Fig. 2c). To examine the life cycle of the breaking wave, we show snapshots within a time window of ±2 days at a 1-day interval.

At 1200 UTC 25 August, the 850-hPa geopotential height shows two lows, L1 and L2, over North America (Fig. 2a). While L1 appears at a higher latitude and has attained a well-defined circulation, L2 is an open system embedded in a moisture plume near the east coast of North America. In this region, the relatively sharp gradients of the 850-hPa geopotential height and the moisture content suggest the presence of a frontal system. In the next 24 h, L2 slowly moves northeastward

but develops rapidly as a moist and warm airstream wraps into its center. By the end of the 24 h, the strength of L2 has exceeded that of L1 (Fig. 2b). Meanwhile, a low-PV tongue develops east of L2 and over the moisture plume, consistent with the amplification of a ridge at the 200-hPa level (not shown).

By 1200 UTC 27 August, the reference time ($T = 0$ h) of wave breaking, the two lower-tropospheric lows have merged (the new low denoted as "L" in Fig. 2c) and traveled northeastward to the open ocean. Meanwhile, the low-PV tongue at the 350-K isentropic surface extends northeastward and contributes to the extensive reversal of PV contour, which exemplifies the pattern of wave breaking. In the following 48 h, the 850-hPa low continues moving northeastward in the extratropics. At lower latitudes, the subtropical high and the 350-K high-PV tongue transport the extratropical dry air southwestward into the tropics. The impacts of similar events on tropical weather have been documented in the companion studies (Zhang et al. 2016, 2017). This study will focus on the extratropical variations in the wave life cycle, which will be analyzed using the composite analysis in the followed sections.

b. *Synoptic evolution of breaking waves: Lead–lag composites*

We next examine the evolution of breaking waves using lead–lag composites (Fig. 3). The reference time ($T = 0$ h) in the lead–lag composites, as described in section 2b, is the 429 time steps when the high-PV tongues of breaking waves are the most extensive. We derive the lead–lag composites by averaging variables leading or lagging the 429 time steps. The lead–lag composites at positive time steps like +96 h are the averages that are 96 h after the reference time. The composites at negative time steps like −96 h are the averages that are 96 h before the reference time. Other than requiring the centroids of the high-PV tongues to appear in the domain of the northwestern Atlantic (Fig. 1b) at $T = 0$ h, the composite analysis imposes no constraints on the location, the configuration, or the propagation of the breaking waves. Despite the large variability among breaking waves, the composite wave shows statistically significant anomalies at both upper and lower levels. The sequence from −96 to +96 h suggests that the primary wave signals start as weak perturbations, develop over North America, peak over the North Atlantic, and decay near western Europe. The life span of the breaking wave is at least 8 days, roughly consistent with that in the past idealized simulations (e.g., Thorncroft et al. 1993; Polvani and Esler 2007).

At the 850-hPa level, a dipole of geopotential height anomalies develops near the Great Lakes region and corresponds to an increasingly sharp gradient of geopotential height between the pair ($T = -96$ to -48 h). The orientation of the dipole is initially northwest–southeast ($T = -96$ to -48 h) but soon rotates anticyclonically as the cyclonic anomalies move northeastward and the anticyclonic anomalies nearly stagnate ($T = -48$ to $+48$ h). The gradual change of the orientation is more evident in the composites that are plotted at shorter time intervals (not shown) and cannot be explained by the interaction of the lower-level cyclone and anticyclone. Instead, the composites suggest that the lower-level cyclone moves toward Greenland ($T = -48$ to 0 h) as a result of the poleward and nonlinear advection by the upper-level ridge and trough anomalies (e.g., Coronel et al. 2015; Tamarin and Kaspi 2016). After reaching the south of Greenland, the lower-level cyclone appears to continue moving eastward, and the associated geopotential height anomalies strengthen by >80% (about 10 m) after merging with a lower-level trough near Iceland ($T = -48$ to 0 h).

At the 200-hPa level, a weak wave train pattern is clear in the midlatitudes before wave breaking ($T = -96$ to 0 h). During the wave life cycle, the most striking feature of the wave train is the amplifying ridge that moves from North America to the North Atlantic. As the baroclinic wave amplifies, the ridge anomalies over the relatively moist regions become about 4 times as strong as the adjacent trough anomalies over the relatively dry regions ($T = 0$ h). The strengthening of ridge-related negative PV anomalies, together with the 3D advection of high PV southeast of the ridge (see section 4a), result in the overturning of PV contours south of the ridge (Figs. 3f–j), a defining feature of Rossby wave breaking. The amplification of the ridge anomalies is broader and more rapid than that of the adjacent trough anomalies. The strong asymmetry of the amplification rates differs from the life cycle of dry baroclinic waves in idealized simulations (e.g., Thorncroft et al. 1993; Polvani and Esler 2007), which instead shows that ridge and trough anomalies grow at more comparable rates. A preference of anticyclone development at the upper level is present in a two-layer moist quasigeostrophic model, and the upper-level anticyclone strengthens with the latent heating (Lapeyre and Held 2004). Thus, the preferred amplification of ridge anomalies may see contributions by moist processes. The possibility will be further explored in section 4.

The flow anomalies of the breaking wave are coupled with anomalies in other atmospheric variables and affect an extensive area. For example, the lower-level cyclone–anticyclone pair that develops over North America affects temperature advection and contributes to a dipole of temperature anomalies ($T = -48$ h). Similarly, the

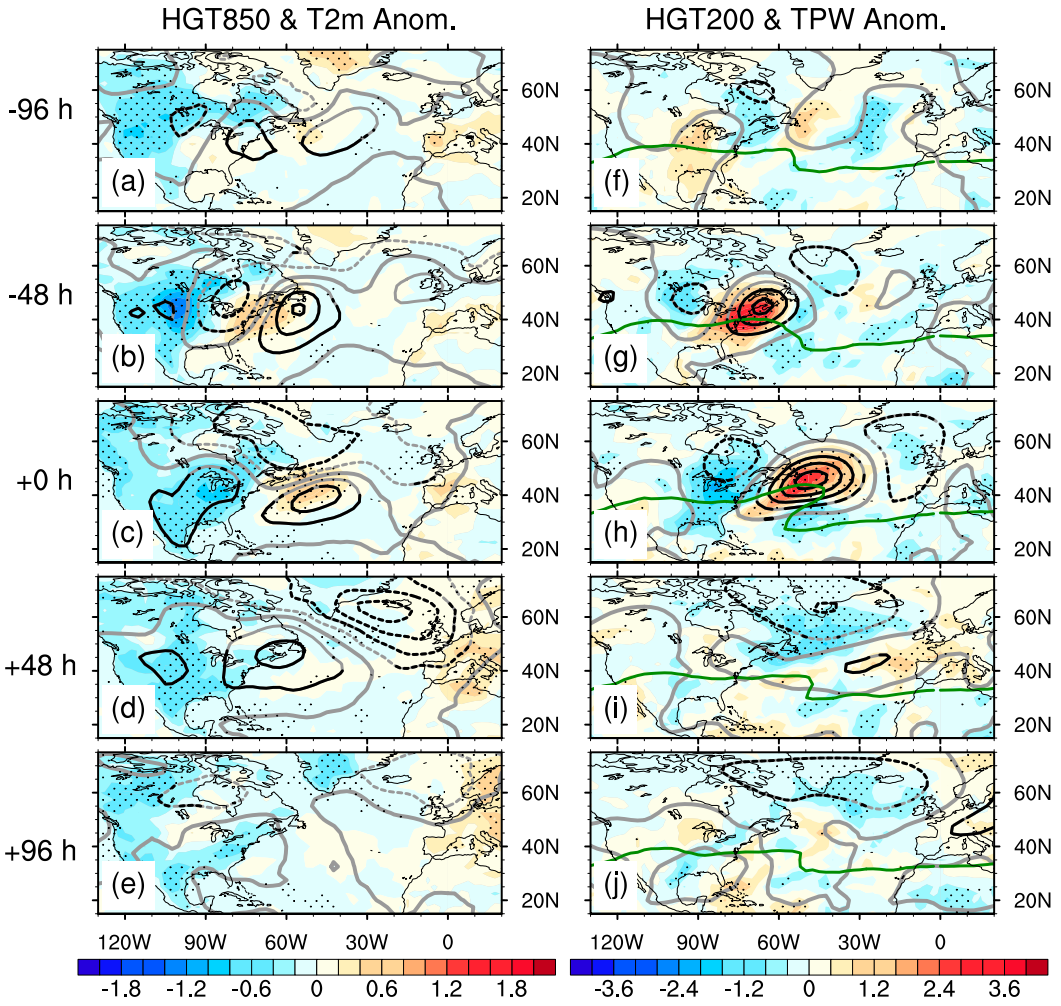

FIG. 3. Composites of breaking waves from $T = -96$ to $+96$ h. (a)–(e) Anomalies of 850-hPa geopotential height (black contours; m) and 2-m temperature (color shading; K). (f)–(j) Anomalies of 200-hPa geopotential height (gray contours; m) and total precipitable water (color shading; kg m^{-2}). (right) The 2.5-PVU contours (green; PVU) on the 350-K isentropic surface outline the breaking wave near $T = 0$ h. The 200- and 850-hPa geopotential height anomalies are contoured at the intervals of 15 and 5 m, respectively; their zero contours are highlighted by boldface font. Signals that pass the 90% confidence level are highlighted with black (contour) and dots (shading). The statistical significance in this figure and the following figures is estimated with the Student's *t* test.

lower-level cyclone over the eastern Atlantic at the late stage of the wave life cycle promotes warm advection and leads to widespread warm anomalies over western Europe ($T = +48$ h). In addition, the near-surface temperature anomalies generally accompany the anomalies of total precipitable water, especially at the developing stage of the breaking wave ($T = -96$ to 0 h). The anomalies are up to 4 mm along the east coast of North America, or 10%–20% of the local background values during July–October. The anomalies associated with breaking waves are also observed in precipitation, sea level pressure, and vertical wind shear (not shown). Compared to the pronounced environmental perturbations in individual cases (e.g., L in Fig. 2), the anomalies in the composites are moderate because the composite averaging smooths out perturbations. Nonetheless, the characteristics of the wave life cycle in the case analysis and the lead–lag composites are generally consistent.

c. *Wave propagation and large-scale environment*

In many modeling studies of wave breaking, baroclinic waves develop from minimal perturbations by converting baroclinic energy within specified domains (e.g., Thorncroft et al. 1993; Polvani and Esler 2007). However, the baroclinic waves in the real world can develop from preexisting upper-level perturbations that move from remote regions (e.g., Petterssen and Smebye 1971). To better assess the wave life cycle in a broader

context, we use the Hovmöller diagram to examine the wave signals in an extended temporal and longitudinal range. The spatial–temporal relation in the Hovmöller diagram follows that in the lead–lag composites. The diagram averages the data between 35° and 55°N and shows the averages in the longitude–time space.

Figure 4 shows that a weak wave train, from about $T = -144$ to 120 h, propagates eastward from the North Pacific to North America, North Atlantic, and Eurasia at a zonal group speed of about 34° longitude per day ($\sim 30\,\mathrm{m\,s^{-1}}$). As suggested by recent studies on the wintertime teleconnection between the North Pacific and the North Atlantic (e.g., Drouard et al. 2015), the downstream propagation suggests that flow perturbations over the North Pacific modulate wave breaking over the North Atlantic. At about $T = -72$ h, a ridge node of the wave train starts to amplify rapidly over North America (near 80°W). The amplifying ridge soon becomes the strongest node of the wave train ($T = -24$ h), and the zonal group speed of the wave packet appear to increase to about 88° longitude per day ($\sim 80\,\mathrm{m\,s^{-1}}$). It is difficult to determine the exact cause of such an increase in the group speed, especially given that the speed values are subject to potential analysis errors. Nonetheless, the zonal group speed is clearly larger than the zonal phase speed, which is about 11° longitude per day ($\sim 10\,\mathrm{m\,s^{-1}}$). The zonal phase speed, rather than the zonal group speed, is close to the moving speed of the lower-level cyclone (Figs. 3a–e), suggesting a coupling between the upper and the lower levels. This suggests that the lower-level cyclone over the eastern Atlantic ($T = 48$ h; Fig. 3d) is a cyclone that moves from the western Atlantic, rather than a new cyclone that develops locally because of the downstream energy dispersion (Simmons and Hoskins 1979; Orlanski and Sheldon 1995).

Consistent with Fig. 3, the Hovmöller diagram also shows the correspondence of flow anomalies and moisture anomalies. More specifically, the strongest anomalies of 200-hPa geopotential height appear about 10° longitude east of the strongest anomalies of total precipitable water (Fig. 4a). A similar relationship of spatial phasing also exists between the anomalies of 200-hPa PV and precipitation (Fig. 4b), even though the precipitation anomalies appear more localized when compared with the anomalies of total precipitable water. Given that the moisture anomalies are coupled with the lower-level temperature and flow anomalies, the spatial phasing can be linked to the westward tilting of geopotential height anomalies with height (e.g., Figs. 3b and 3g), which is an essential characteristic of baroclinic waves in both the dry (e.g., Eady 1949) and moist (e.g., Moore and Montgomery 2004) environment. The spatial phasing is also consistent with the Sutcliffe–Petterssen

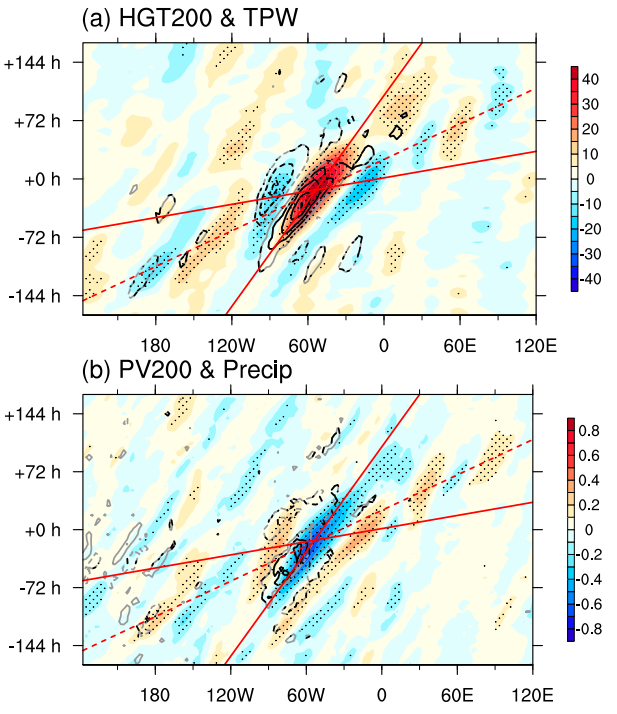

FIG. 4. Hovmöller diagram of the anomalies (average over 35°–55°N) associated with breaking waves. (a) Anomalies of 200-hPa geopotential height (shading; m) and total precipitable water (gray contour; mm). (b) Anomalies of 200-hPa PV (shading; PVU) and precipitation (gray contour; mm). The total precipitable water and precipitation anomalies are contoured at the intervals of 0.5 and 0.1 mm, respectively. The zero contours of geopotential height and PV are omitted for clarity of the figure. Signals that pass the 90% confidence level are highlighted with black (contour) and dots (shading). The subjective reference lines (red) help determine the group speed and the phase speed of the wave train.

development theory, in which cyclogenesis involves a positive feedback between the lower-level thermal advection and the upper-level vorticity advection (Sutcliffe and Forsdyke 1950; Pettersen 1956). In particular, the quasigeostrophic forcing for ascent related to the weak upper-level trough (near 100°W) may play a role in initiating precipitation around $T = -72$ h. Nonetheless, the strongest flow anomalies associated with the amplifying upper-level ridge appear near $T = 0$ h and lag the strongest anomalies of moisture and precipitation by about 18 h, suggesting that diabatic processes feed back to the flow during the wave life cycle. The next section will investigate the role of diabatic processes in the development of breaking waves.

4. Diabatic impacts on wave life cycle

The impacts of diabatic processes on the lower-level flow, such as the cyclone intensification (e.g., Whitaker and Davis 1994; Parker and Thorpe 1995) and the

cyclone motion (e.g., Coronel et al. 2015; Tamarin and Kaspi 2016), have been extensively investigated from the PV perspective. The physical mechanisms described in the earlier studies can satisfactorily explain the low-level flow evolution. Here we mainly focus on how diabatic processes facilitates upper-level wave breaking, which to our knowledge has not been thoroughly studied.

a. PV budget analysis

For the sake of brevity, we select $T = -48$ h, when precipitation is relatively heavy (Fig. 4), and analyze the tendency of 200-hPa PV caused by the 3D advection and the diabatic production [see Eq. (2)]. The 3D advection is further separated into the horizontal advection and the vertical advection; the PV production by diabatic heating, as introduced in section 2d, is separated into two parts contributed by the parameterized model physics and the data assimilation, respectively. This approach helps analyze how different physical and model processes affect the upper-level PV, and we show the results of advection terms and diabatic terms separately in Figs. 5 and 6.

The PV tendency caused by the 3D advection (Fig. 5a) is dominated by a dipole pattern near the upper-level ridge. Consistent with the eastward motion of the upper-level ridge, the positive PV tendency prevails on the west side of the upper-level ridge while the negative PV tendency dominates the east side. The maximum strength of PV tendency is about 0.3 PVU $(6\,\text{h})^{-1}$ on both sides of the ridge, but the positive PV tendency on the west side is slightly weaker. The difference is related to the contribution by the vertical advection on the northwestern side of the upper-level ridge (Fig. 5c). The contribution by the vertical advection is weaker than the horizontal advection (Fig. 5b) but still statistically significant from being zero. Notably, the negative vertical advection counteracts the positive tendency by the horizontal advection in the western part of the upper-level ridge. The negative vertical advection thus helps amplify the upper-level ridge and slow down its eastward propagation. The negative vertical advection, given that PV generally increases with height within the upper troposphere and lower stratosphere, can be largely explained by the upward motion in the precipitating region [not shown; see Fig. 4 in Zhang et al. (2017)]. Similarly, the weak positive PV tendency southeast of the ridge, which moderately strengthens the high-PV tongue associated with wave breaking, can be attributed to the local downward motion (not shown).

Like the vertical advection, diabatic heating also contributes to negative PV tendency on the northwestern side of the upper-level ridge (Fig. 6a). The negative

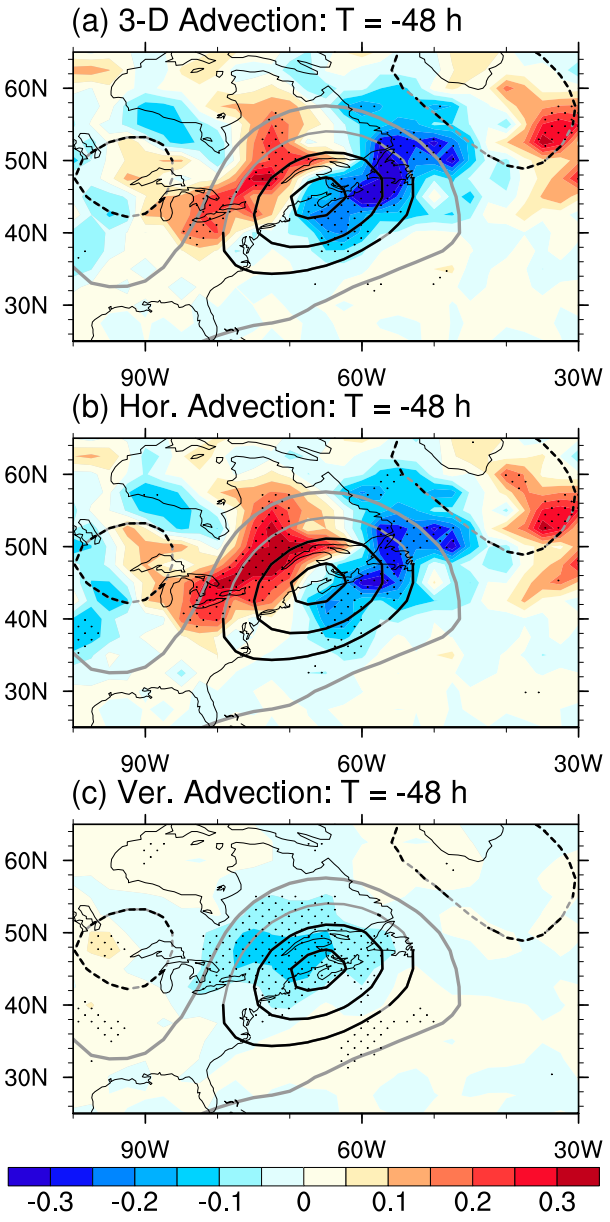

FIG. 5. The 200-hPa PV tendency [shading, PVU $(6\,\text{h})^{-1}$] by the advection at $T = -48$ h. The contributions by (a) the 3D advection, (b) the horizontal advection, and (c) the vertical advection are shown. The gray contours show the anomalies of 200-hPa geopotential height, with the signals that pass the 90% confidence level highlighted with the black color. All other settings follow those of Fig. 3.

PV tendency, which amplifies the upper-level ridge, likely arises from the moist updraft and the release of latent heat associated with the precipitation anomalies. As the heating tends to maximize in the midtroposphere, the static stability in the upper troposphere likely decreases, and the change is accompanied by negative PV anomalies (e.g., Raymond and Jiang 1990; Chagnon and Gray 2009; Rowe and Hitchman 2015). The negative PV

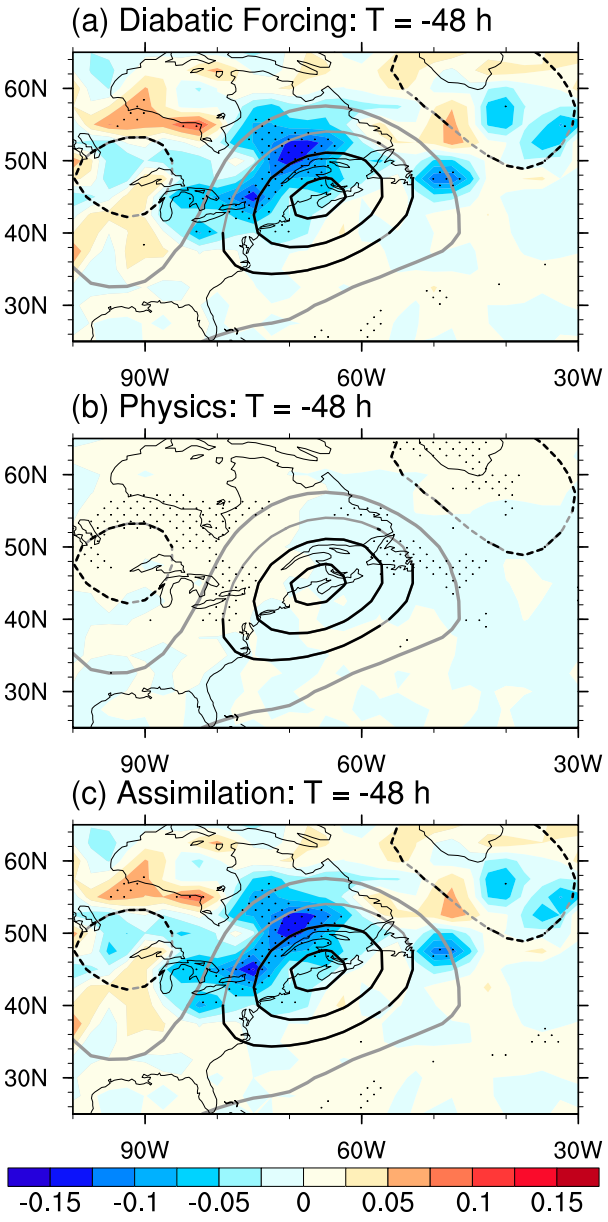

FIG. 6. As in Fig. 5, but for the PV tendency by the diabatic production. The contributions by (a) the total diabatic heating, (b) the parameterized model physics, and (c) the data assimilation are shown

tendency is notably stronger than the positive tendency in the nearby nonprecipitating trough regions (cf. Figs. 3 and 4), likely because precipitation contributes to relatively intense vertical motion and diabatic heating. The difference in the PV tendency is consistent with that the ridge anomalies gradually become stronger than the trough anomalies ($T = -96$ to 0 h, Fig. 4).

Interestingly, further analyses of the diabatic PV tendency suggest that the parameterized model physics (Fig. 6b) contributes much less than the data assimilation does (Fig. 6c). Consistent with the weak PV tendency in Fig. 6b, the parameterized model physics tends to produce very weak diabatic heating near the 200-hPa level (not shown). In contrast, the PV tendency by the data assimilation (Fig. 6c) attains large values and shows a coherent pattern in the precipitating region, namely the northeast of North America (Fig. 4b). The fact that the coherent pattern is present in the precipitating region, rather than the adjacent regions, suggests that the assimilation "corrections"—and thus model errors—are linked to moist diabatic processes. Admittedly, the PV tendency in Fig. 6c includes errors from estimating the residuals of temperature tendency, and it is difficult to directly validate the diabatic heating and its impacts in the reanalysis against the real state of the upper troposphere and lower stratosphere. However, previous studies reported large uncertainties of the local budget of diabatic heating in this layer and inferred that the forecast models used to generate the reanalysis datasets might suffer from deficient physics parameterizations (Fueglistaler et al. 2009; Wright and Fueglistaler 2013).

We next move beyond $T = -48$ h and evaluate the relative importance of the 3D advection and the diabatic production of PV in the development of the upper-level ridge. Based on the characteristics of the 200-hPa ridge at $T = 0$ h, we set up a moving domain (35°–55°N, 65°–35°W at $T = 0$ h) that slides into the channel of 35°–55°N. To characterize the evolution of the upper-level ridge, the center of the moving domain at each time step ($T = -96$ to $+96$ h) is determined using the zonal phase speed of the upper-level ridge. The phase speed is estimated using the Hovmöller diagram (Fig. 4) and is about 11° longitude per day ($\sim 10\ \mathrm{m\ s^{-1}}$). Within the moving domain, we calculate the averages of key variables and show their time series (Fig. 7). Before introducing the results, we note that moderate changes of the settings of the moving domain, such as varying its latitudinal or longitudinal ranges by 5°, do not affect the results to be presented.

Figure 7a shows that the increase of precipitation precedes the development of the upper-level ridge by about 24 h, and the time when the ridge anomalies reach the greatest strength roughly corresponds to the time of wave breaking ($T = -0$ h). The characteristics, consistent with Figs. 3 and 4, suggest that our approach of tracking the upper-level ridge reasonably describes its development and the associated precipitation anomalies, lending confidence to our evaluation of the PV tendency related to the 3D advection and the diabatic production (Fig. 7b). A comparison of Figs. 7a and 7b suggests that the two terms of PV tendency reasonably describe the PV changes in the moving domain. During

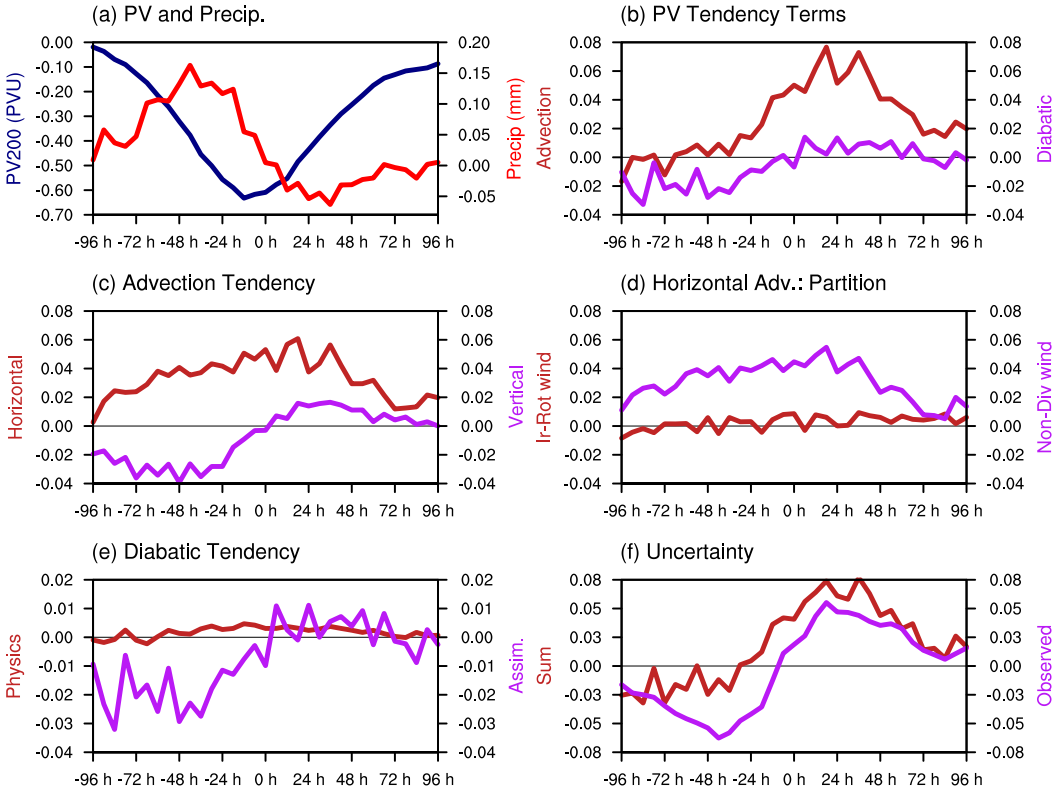

FIG. 7. Time series of key variables in the moving domain that characterizes the 200-hPa ridge (see the text for details). (a) 200-hPa PV (blue; PVU) and precipitation (red; mm). (b) PV tendency by the 3D advection (brown) and the diabatic production (purple). (c) PV tendency by the horizontal (brown) and the vertical (purple) advection. (d) The horizontal advection of PV by the irrotational wind (brown) and the nondivergent wind (purple) components. (e) PV tendency by the parameterized physics (brown) and the data assimilation (purple). (f) Total PV tendency estimated by summing the tendency terms (brown) and by differencing the values of PV (purple). The unit of all the PV tendency terms is PVU $(6\,\mathrm{h})^{-1}$. To maximize details, the scaling of vertical axes in (e) and (f) differs from that in (b)–(d).

the wave life cycle, the 3D advection does not strongly affect the PV associated with the moving ridge until about $T = -24$ h, when the horizontal advection on the northwestern side of the ridge becomes relatively strong (not shown). As the ridge moves eastward and the trough northwest of the ridge deepens (Fig. 3i), the positive contribution by the 3D advection increases and peaks during $T = 0$ to 48 h (Fig. 7b), corresponding to the rapid weakening of the upper-level ridge. However, the ridge amplification is mainly related to the diabatic production (Fig. 7b), which dominates the PV tendency during $T = -72$ to -36 h. The period corresponds to active precipitation (Fig. 7a) and features the diabatic production of PV that is consistently negative. After $T = -36$ h, the contribution by diabatic production weakens with the precipitation and remains close to zero after wave breaking.

We further examine how the individual terms in Eq. (3) contribute to the PV tendency. Figure 7c suggests that the strong tendency contributed by the horizontal and the vertical advection offsets each other before $T = -24$ h, keeping the contribution by the 3D advection close to zero. After $T = -24$ h, the contribution by the vertical advection switches from negative to positive and weakens to <30% of the contribution by the horizontal advection. The positive tendency by the horizontal advection is related to the advection of PV across the boundaries of the moving domain, whose contribution can deviate from zero because of an asymmetry of the perturbed flow (Fig. 5b). The positive tendency is also consistent with the study of Swenson and Straus (2017), which noted that the transient eddy momentum and heat fluxes associated with wave breaking opposes the ridge amplification and contributes to the ridge decay. Following earlier studies (e.g., Teubler and Riemer 2016), the horizontal advection of PV is partitioned into the part contributed by the irrotational wind and the part contributed by the nondivergent wind (Fig. 7d).

The latter can be associated with diabatic processes, but its contribution to the PV tendency is close to zero, much weaker than the other terms modulated by diabatic processes. Notably, the vertical advection (Fig. 7c), another term related to the moist updrafts and thus the diabatic impact, is about 150% as strong as the contribution by the diabatic production (Fig. 7b). On other hand, the diabatic production is not strongly affected by the parameterized physics but is instead dominated by the assimilation term (Fig. 7e). The phasing of the assimilation term is consistent with that of the precipitation, suggesting that the assimilation term is unlikely dominated by random calculation errors in the PV budget analysis.

Because of the coarse spatial and temporal resolution of our data, we expect some uncertainty of the PV budget analysis. We estimate the uncertainty by comparing the PV tendency estimated with two methods: 1) summing of the 3D advection and the diabatic production ("sum"), and 2) differencing the observed PV values ("observed"). We consider the latter as the truth and compare it with the sum of the tendency terms. As shown in Fig. 7f, a comparison of the estimated PV tendency suggests that the sum has a consistent and positive bias during $T = -72$ to 48 h. In particular, the sum of the PV budget terms underestimates the negative PV tendency related to the ridge amplification ($T = -72$ to -24 h) by about 0.04 PVU $(6\,\text{h})^{-1}$. Assuming that the signs of the PV tendency terms are reliable, correcting the bias would require a reduction the positive horizontal advection [~0.04 PVU $(6\,\text{h})^{-1}$] by ~100%, or increasing the negative PV tendency terms [~0.05 PVU $(6\,\text{h})^{-1}$] by ~80%.

Overall, the PV budget analysis suggests that the PV tendency related to the horizontal and the vertical advection are large, but their contributions offset each other when precipitation is active. Consequently, the 3D advection does not dominate the intensity changes of the ridge until after the wave breaks. The amplification of the upper-level ridge, which is underestimated in the PV budget analysis, appears to result from the vertical advection and the diabatic production of PV.

b. *Cross-sectional and trajectory analysis*

The estimate of the diabatic production term in the PV budget analysis has at least two limitations: 1) the budget analysis has substantial uncertainties during the period of wave amplification and active precipitation; and 2) the term is dominated by the data assimilation, which is not explicitly related to physical processes. To support the connection between the negative PV anomalies to diabatic processes, we now carry out cross-section analyses of the breaking waves. For the brevity of discussion, we focus on $T = 0$ h and build the composite cross section of PV and potential temperature over the range of 35°–65°W (Fig. 8), which covers the primary PV anomalies associated with wave breaking. Near 45°N, the negative PV anomalies related to the upper-level ridge extends from the lower stratosphere to the upper troposphere, with the strongest anomalies (close to −1 PVU) located near the tropopause (2-PVU contour). Even though the composite approach likely smooths out some finescale structures, the strength of the negative PV anomalies implies possible folding of the tropopause. On the flanks of the negative PV anomalies, PV values increase near the tropopause at both 30° and 60°N. These PV anomalies are coupled with the lower-troposphere anomalies, including those near 45°N that correspond to the cyclone–anticyclone pair examined in section 3.

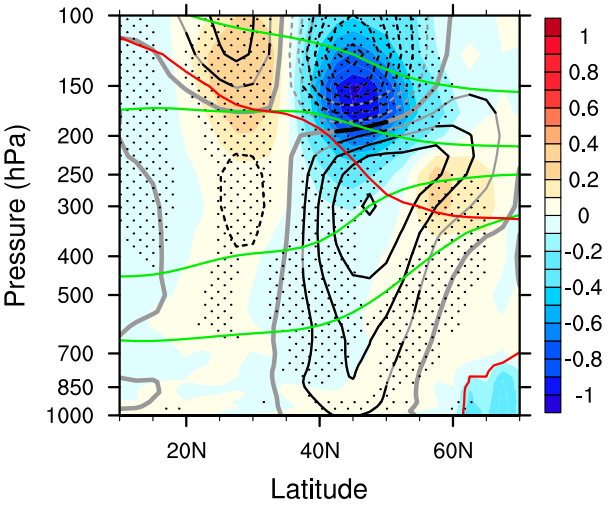

FIG. 8. Zonal average (35°–65°W) of the anomalies of potential temperature (gray contours) and potential vorticity (PV; color shading) that are associated with the breaking wave. The climatological mean of potential temperature (315-, 330-, 350-, and 385-K contours in green) and the climatological mean PV (2-PVU contour in red) are overlaid. The anomalies of potential temperature are plotted at the interval of 0.5 K, with the zero contour thickened and the positive (negative) contours plotted with thin solid (dashed) lines. Signals that pass the 90% confidence level are highlighted by black (contour) and dots (shading).

PV anomalies, as discussed in Martin (2006), are associated with anomalous static stability. Consistently, the negative PV anomalies near 45°N are accompanied by potential temperature anomalies that are positive below and negative above. The positive anomalies of potential temperature anomalies are vertically aligned near 45°N and show slantwise characteristics at higher latitudes, while the negative anomalies of potential temperature are almost concentrated above the deepest positive anomalies. The overall pattern is consistent

with that of the temperature perturbations associated with the breaking waves over the North Pacific (Strong and Magnusdottir 2009), even though their dataset and compositing approach differ from ours. The robust anomalies of potential temperature are related to anomalous static stability near the dynamic tropopause, which are consistent with the negative PV anomalies near 45°N and positive PV anomalies near 30° and 60°N. The coherent structure is present at other time steps when the upper-level ridge is distinct. Next, we will link the anomalies of potential temperature to diabatic heating using the trajectory analysis.

We carry out backward trajectory analysis for air parcels at 125- and 300-hPa levels (hereafter the 125- and the 300-hPa groups), where the anomalies of potential temperature are the strongest ($T = 0$ h). When the tracking is initialized, the air parcels are on the 2.5° grid of the reanalysis data and located in the domain of 35°–55°N, 65°–35°W. To ensure that the analyzed air parcels are directly related to the ridge, we calculate the anomalies of the 200-hPa PV at $T = 0$ h and only analyze the air parcels that are right above or below these negative PV anomalies. These air parcels are tracked for each breaking wave individually, but the characteristics of the parcels are analyzed collectively. Like the analyses of the PV tendency, moderate changes of the domain do not undermine the findings to be presented. The probability density functions (PDFs) of the ridge-associated air parcels are shown in Fig. 9. At $T = -96$ h (Fig. 9a), a majority of the parcels in the 125-hPa level group are located over the western coast of North America, while their 300-hPa counterparts generally appear over North America. By $T = -48$ h (Fig. 9b), the air parcels in the two groups begin to meet near the eastern coast of North America, where the precipitation is active (Fig. 4b). The spatial overlapping of the air parcels and the precipitation is consistent with the expectation that the diabatic processes related to precipitation may modify the potential temperature of the tracked air parcels.

We now use the joint PDF to link the potential temperature changes ($T = -96$ to 0 h) of the air parcels to their vertical displacement ($T = -96$ to 0 h), as well as the anomalies of potential temperature ($T = 0$ h) relative to the seasonally adjusted long-term mean. Figures 10a and 10c show the joint PDF of the potential temperature changes and the vertical displacement of the air parcels. The two variables show a nearly linear relation for the air parcels in the 300-hPa group, with most air parcels originating between the 200- and the 700-hPa levels. The linear relation in the 300-hPa group slopes at about 0.06 K hPa^{-1}, a value comparable to the mean environmental lapse rate within 35°–55°N (Fig. 8), implying that

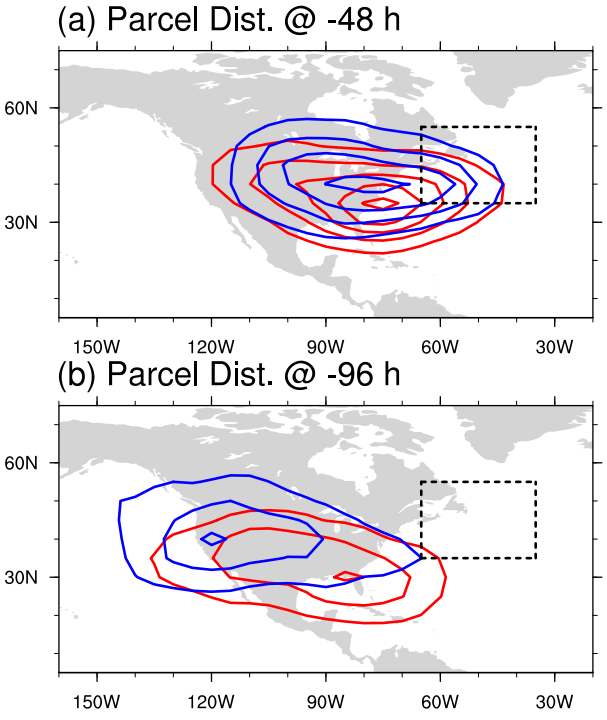

FIG. 9. Distributions of the ridge-associated air parcels at different time steps. The backward tracking is initialized at $T = 0$ h for the air parcels at the 125-hPa (blue) and the 300-hPa (red) levels. At $T = 0$ h, the analyzed air parcels have to be located in the ridge region (black dashed lines) and right above or below the negative PV anomalies at 200 hPa. We show the distributions of these air parcels at (a) $T = -48$ and (b) $T = -96$ h. The PDFs are contoured with the interval of 5×10^{-3} on a 5° grid.

the relation can be explained by the displacement of heated parcels in a stratified atmosphere. Such a linear relation is absent in the 125-hPa group, in which air parcels show much smaller vertical displacement in the isobaric coordinates. The comparison of the 300-hPa and the 125-hPa groups also suggests that the air parcels in the 300-hPa group more likely experience strong latent heating associated with ascending motion (57%), while their 125-hPa counterparts generally experience net cooling (67%). The signs, locations, and intensities of the diabatic heating are consistent with the latent heating in the troposphere and the radiative cooling in the lower stratosphere. Figures 10b and 10d show the joint PDF of the potential temperature changes of the air parcels ($T = -96$ to 0 h) and the anomalies of potential temperature at $T = 0$ h. As expected, most air parcels in the 300-hPa group are associated with positive anomalies of potential temperature at $T = 0$ h, and about two-thirds of these parcels experience net heating during $T = -96$ to 0 h. Similarly, most air parcels in the 125-hPa group are associated with negative anomalies of potential temperature at $T = 0$ h, and over two-thirds of

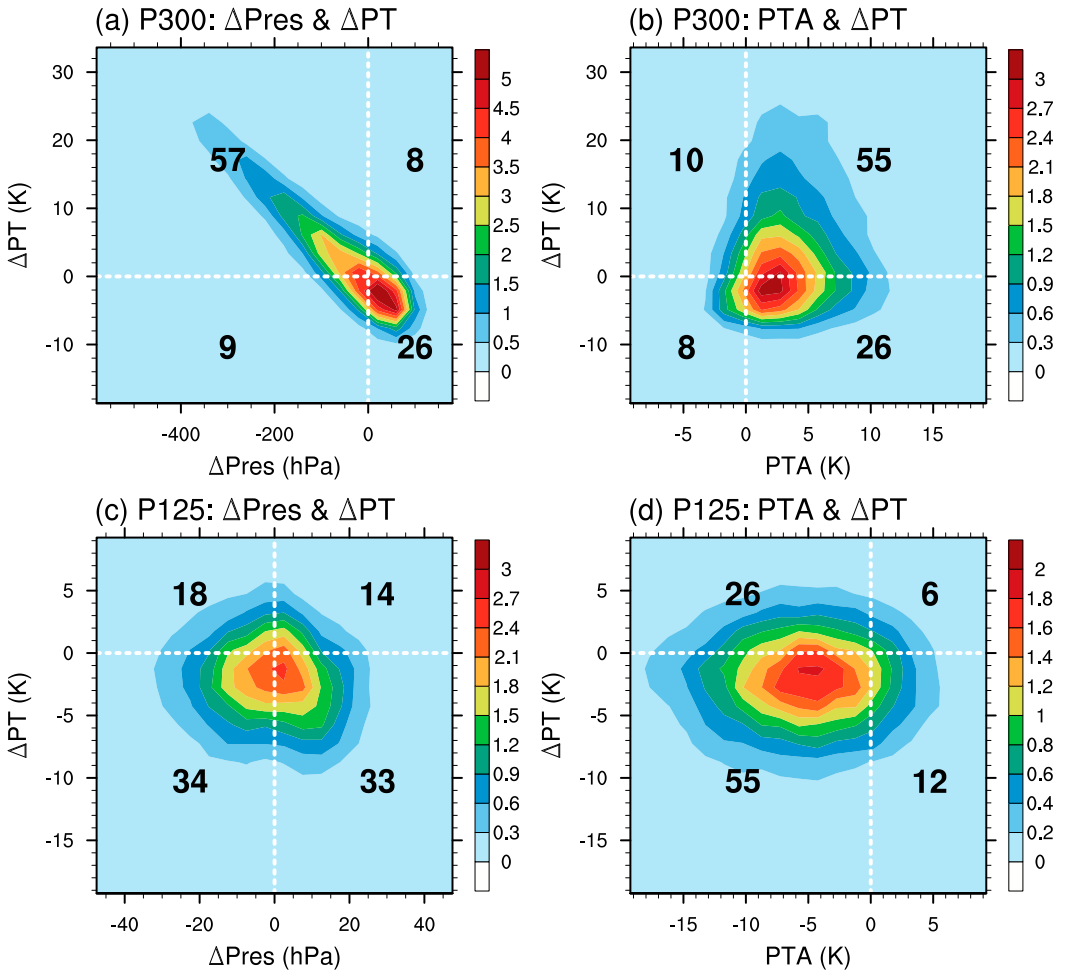

FIG. 10. Diabatic heating experienced by the ridge-associated air parcels from $T = -96$ to $T = 0$ h. (a),(c) PDFs of the potential temperature changes (ΔPT) and the vertical displacement (ΔPres) experienced by air parcels in the 300- and 125-hPa groups (see the text for more details). (b),(d) PDFs of the potential temperature changes and the potential temperature anomalies (PTA) at $T = 0$ h. All the changes are calculated as the state at $T = 0$ h minus the state at $T = -96$ h, so the positive values along the vertical axes of (a)–(d) and the negative values along the horizontal axes of (a),(c) correspond to heating and ascending, respectively. The white dashed lines separate the domains into four quadrants, and the sums of the PDFs in each quadrant are shown at the corresponding quadrant center.

them experience net cooling during $T = -96$ to 0 h. Taken together, the analyses suggest that the diabatic heating during the early stage of the wave life cycle is consistent with the reduced static stability near the tropopause (Fig. 8), and hence diabatic processes are crucial for the amplification of the upper-level ridge that culminates in wave breaking.

5. Summary and discussion

Previous studies suggest that understanding the life cycle of breaking waves is valuable for weather forecasting and subseasonal-to-seasonal prediction during the warm season. This study analyzes anticyclonic wave breaking in the North Atlantic basin. The wave breaking signals at the upper level are coupled with a dipole of geopotential height anomalies and moist anomalies at the lower level. Moreover, the breaking waves are related to a Rossby wave dispersion from the North Pacific. When the wave train approaches the east coast of North America, a ridge develops rapidly over a poleward stream of warm and moist air. The rapid ridge amplification, as well as the concomitant PV advection on the southeast side of the ridge, eventually overturns PV contours and promotes Rossby wave breaking. Notably, the ridge anomalies are about 4 times as strong as the adjacent trough anomalies that develop over the relatively dry regions. The preferred amplification of the

upper-level ridge differs from that in the dry idealized simulations, which features a comparable amplification of ridge and trough anomalies, and suggests the influence of moist diabatic processes.

We link the upper-level ridge amplification to the diabatic heating using the PV tendency analyses and the trajectory analysis of the ridge-related air parcels. The PV tendency analyses suggest that the horizontal advection of PV largely dictates the movement of the upper-level ridge and explains its decay after wave breaking. In particular, the horizontal advection by the perturbed flow is large but opposes the ridge amplification. The opposing effect of the horizontal advection is overpowered by the vertical advection and the diabatic production of PV, which account for nearly all the ridge-related decrease of PV before wave breaking. Although the PV budget analysis has uncertainties because of the data resolution and our composite methodology, the finding is corroborated by the cross-sectional and Lagrangian trajectory analysis. These analyses suggest that the ridge-related anomalies of PV are associated with a decrease of static stability near the tropopause, which can be attributed to the heating of tropospheric air and the cooling of stratospheric air by diabatic processes.

The findings of the wave life cycle and the diabatic heating can be generalized for anticyclonic wave breaking over the other ocean basins and for different seasons. Compositing breaking waves in different domains can result in moderately different the patterns during the wave life cycle, but we consistently find that that diabatic processes amplify the upper-level ridge and promote anticyclone wave breaking (not shown). We also examined cyclonic wave breaking over the oceans, which tend to occur less frequently and at higher latitudes (not shown). Despite the relatively low moisture content at higher latitudes, diabatic heating seems to remain important for the overturning of PV contours by contributing to the negative PV anomalies that wrap cyclonically around the high-PV cutoffs (e.g., Posselt and Martin 2004; Tamarin and Kaspi 2016). In regions where moisture supply is more limited, the diabatic heating probably cannot effectively amplify the upper-troposphere ridge and contribute to wave breaking. Coincidently, most wave breaking in the upper troposphere occur over the ocean rather than the land (e.g., Abatzoglou and Magnusdottir 2006; Wernli and Sprenger 2007).

Our emphasis on moisture and diabatic processes echoes with the notion of ''monsoon wave breaking'' in Hitchman and Huesmann (2007). The study suggested that the monsoon convection contributes to an upper-level anticyclone that helps overturn PV contours. The wave breaking mechanism involved with the monsoon-related quasi-stationary wave resembles the mechanism involved with the transient moving waves. The relation between diabatic processes and wave breaking were also discussed by Madonna et al. (2014) with the terms ''warm conveyor belt'' and ''PV streamers,'' which roughly correspond to the moist precipitating band and the upper-level equatorward intrusions in our discussion. Madonna et al. (2014) identified only 10 co-occurrence events over the North Atlantic during June–November of 1989–2009 and suggested that merely about 15% of all PV streamers in their datasets co-occur with warm conveyor belts. However, we note that the study used a very strict criterion to define the warm conveyor belt, which considered only the cases with the most intense ascending (''exceeding 600 hPa within 2 days'') from the lowermost troposphere. The criterion excludes a large number of cases with moderate ascending, leaving most cases in this study (Fig. 10a) unaccounted. Therefore, the statistics in Madonna et al. (2014) emphasizes a fraction of wave breaking events, which are linked to strong warm conveyor belts, and does not necessarily conflict with our findings about the diabatic contribution to wave breaking.

Some of our analyses admittedly have potential limitations that need further remarks. Because of the large variability among breaking waves (Fig. 1b), the anomalies analyzed in this study often appear much weaker than those in individual cases and do not always have high statistical significance. The large variability may also attenuate the signals that are away from the reference time and the domain of interest, potentially distorting the relative strength of flow anomalies in our composite analyses, such as the upper-level ridge and troughs in Figs. 3f–j. In addition, the relatively low temporal and spatial resolutions of the reanalysis data may affect the accuracy of our trajectory analysis. Although we did not see any obvious signs that suggest the limitations have undermined our main findings, one may need to treat some quantitative aspects of our results with caution. We hope that future modeling studies may help to test our findings and build a better theoretical understanding of Rossby wave breaking.

The upper-level wave packet ($T = -144$ to $+144$ h, Fig. 4) suggests that the breaking waves and their downstream influences may be predictable with a lead time up to about 14 days. Nonetheless, the analyses of the diabatic modification of PV (Fig. 6) suggests that the parameterized model physics, at least the version used by the ERA-Interim, may contribute to errors in forecasting the flow structure at some levels near the tropopause. In addition, our companion study (Li et al. 2017, manuscript submitted to *J. Climate*) suggests wave breaking is associated with low skills of medium-range

weather forecasts in NCEP's Global Ensemble Forecasting System reforecast (Hamill et al. 2013). Some studies also suggest that the biases related to breaking waves affect the ECMWF operational models (Wiegand and Knippertz 2014) and the simulation of midlatitude jet streams in climate models (Lu et al. 2015). Some earlier studies also suggest that the model errors can arise from difficulties in representing the interactions between moist diabatic processes and upper-level flow (e.g., Dickinson et al. 1997; Brennan and Lackmann 2005; Zhang et al. 2007; Boettcher and Wernli, 2011; Rodwell et al. 2013), consistent with our emphasis on the importance of diabatic processes for wave breaking. By improving the understanding of Rossby wave breaking that occurs in the real world, we hope that this study may help to stimulate future studies and lead to better predictions of weather and climate during the warm season.

Acknowledgments. The study is supported by NOAA Grants NA15NWS4680007 and NA16OAR4310080, and NRL Grant N00173-15-1-G004. We thank David Schultz, and three anonymous reviewers for thoughtful suggestions, which helped to improve the presentation of our results. We are grateful to Bob Rauber and Lei Wang for the stimulating discussions in the early phase of the study, and to Kai Zhang for the technical insights about the diabatic heating data in the ERA-Interim. We acknowledge the NCAR/CISL for providing computing resources and the ECMWF for making the ERA-Interim publicly available (http://apps.ecmwf.int/datasets/).

REFERENCES

Abatzoglou, J. T., and G. Magnusdottir, 2006: Planetary wave breaking and nonlinear reflection: Seasonal cycle and interannual variability. *J. Climate*, **19**, 6139–6152, https://doi.org/10.1175/JCLI3968.1.

Appenzeller, C., and H. C. Davies, 1992: Structure of stratospheric intrusions into the troposphere. *Nature*, **358**, 570–572, https://doi.org/10.1038/358570a0.

Archambault, H. M., D. Keyser, L. Bosart, C. A. Davis, and J. M. Cordeira, 2015: A composite perspective of the extratropical flow response to recurving western North Pacific tropical cyclones. *Mon. Wea. Rev.*, **143**, 1122–1141, https://doi.org/10.1175/MWR-D-14-00270.1.

Bentley, A., D. Keyser, and L. Bosart, 2016: A dynamically based climatology of subtropical cyclones that undergo tropical transition in the North Atlantic basin. *Mon. Wea. Rev.*, **144**, 2049–2068, https://doi.org/10.1175/MWR-D-15-0251.1.

——, L. Bosart, and D. Keyser, 2017: Upper-tropospheric precursors to the formation of subtropical cyclones that undergo tropical transition in the North Atlantic basin. *Mon. Wea. Rev.*, **145**, 503–520, https://doi.org/10.1175/MWR-D-16-0263.1.

Berrisford, P., and Coauthors, 2011: The ERA-Interim archive, version 2.0. ERA report series, Tech. Rep. 1, ECMWF, 23 pp.

Boettcher, M., and H. Wernli, 2011: Life cycle study of a diabatic Rossby wave as a precursor to rapid cyclogenesis in the North Atlantic—Dynamics and forecast performance. *Mon. Wea. Rev.*, **139**, 1861–1878, https://doi.org/10.1175/2011MWR3504.1.

Brennan, M. J., and G. M. Lackmann, 2005: The influence of incipient latent heat release on the precipitation distribution of the 24–25 January 2000 U.S. East Coast cyclone. *Mon. Wea. Rev.*, **133**, 1913–1937, https://doi.org/10.1175/MWR2959.1.

Chagnon, J. M., and S. L. Gray, 2009: Horizontal potential vorticity dipoles on the convective storm scale. *Quart. J. Roy. Meteor. Soc.*, **135**, 1392–1408, https://doi.org/10.1002/qj.468.

——, ——, and J. Methven, 2013: Diabatic processes modifying potential vorticity in a North Atlantic cyclone. *Quart. J. Roy. Meteor. Soc.*, **139**, 1270–1282, https://doi.org/10.1002/qj.2037.

Coronel, B., D. Ricard, G. Rivière, and P. Arbogast, 2015: Role of moist processes in the tracks of idealized midlatitude surface cyclones. *J. Atmos. Sci.*, **72**, 2979–2996, https://doi.org/10.1175/JAS-D-14-0337.1.

Davis, C. A., and L. F. Bosart, 2004: The TT problem: Forecasting the tropical transition of cyclones. *Bull. Amer. Meteor. Soc.*, **85**, 1657–1662, https://doi.org/10.1175/BAMS-85-11-1657.

Dee, D. P., and Coauthors, 2011: The ERA-Interim reanalysis: Configuration and performance of the data assimilation system. *Quart. J. Roy. Meteor. Soc.*, **137**, 553–597, https://doi.org/10.1002/qj.828.

Dickinson, M. J., L. F. Bosart, W. E. Bracken, G. J. Hakim, D. M. Schultz, M. A. Bedrick, and K. R. Tyle, 1997: The March 1993 Superstorm cyclogenesis: Incipient phase synoptic- and convective-scale flow interaction and model performance. *Mon. Wea. Rev.*, **125**, 3041–3072, https://doi.org/10.1175/1520-0493(1997)125<3041:TMSCIP>2.0.CO;2.

Drouard, M., G. Rivière, and P. Arbogast, 2015: The link between the North Pacific climate variability and the North Atlantic Oscillation via downstream propagation of synoptic waves. *J. Climate*, **28**, 3957–3976, https://doi.org/10.1175/JCLI-D-14-00552.1.

Eady, E. T., 1949: Long waves and cyclone waves. *Tellus*, **1**, 33–52, https://doi.org/10.3402/tellusa.v1i3.8507.

Fitzpatrick, P. J., J. A. Knaff, C. W. Landsea, and S. V. Finley, 1995: Documentation of a systematic bias in the aviation model's forecast of the Atlantic tropical upper-tropospheric trough: Implications for tropical cyclone forecasting. *Wea. Forecasting*, **10**, 433–446, https://doi.org/10.1175/1520-0434(1995)010<0433:DOASBI>2.0.CO;2.

Franzke, C., S. Lee, and S. B. Feldstein, 2004: Is the North Atlantic Oscillation a breaking wave? *J. Atmos. Sci.*, **61**, 145–160, https://doi.org/10.1175/1520-0469(2004)061<0145:ITNAOA>2.0.CO;2.

Fueglistaler, S., B. Legras, A. Beljaars, J. J. Morcrette, A. Simmons, A. M. Tompkins, and S. Uppala, 2009: The diabatic heat budget of the upper troposphere and lower/mid stratosphere in ECMWF reanalyses. *Quart. J. Roy. Meteor. Soc.*, **135**, 21–37, https://doi.org/10.1002/qj.361.

Funatsu, B. M., and D. W. Waugh, 2008: Connections between potential vorticity intrusions and convection in the eastern tropical Pacific. *J. Atmos. Sci.*, **65**, 987–1002, https://doi.org/10.1175/2007JAS2248.1.

Galarneau, T. J., R. McTaggart-Cowan, L. F. Bosart, and C. A. Davis, 2015: Development of North Atlantic tropical disturbances near upper-level potential vorticity streamers. *J. Atmos. Sci.*, **72**, 572–597, https://doi.org/10.1175/JAS-D-14-0106.1.

Grams, C. M., and H. M. Archambault, 2016: The key role of diabatic outflow in amplifying the midlatitude flow: A representative case study of weather systems surrounding western

North Pacific extratropical transition. *Mon. Wea. Rev.*, **144**, 3847–3869, https://doi.org/10.1175/MWR-D-15-0419.1.

Hamill, T. M., G. T. Bates, J. S. Whitaker, D. R. Murray, M. Fiorino, T. J. Galarneau, Y. Zhu, and W. Lapenta, 2013: NOAA's second-generation global medium-range ensemble reforecast dataset. *Bull. Amer. Meteor. Soc.*, **94**, 1553–1565, https://doi.org/10.1175/BAMS-D-12-00014.1.

Hanley, D., J. Molinari, and D. Keyser, 2001: A composite study of the interactions between tropical cyclones and upper-tropospheric troughs. *Mon. Wea. Rev.*, **129**, 2570–2584, https://doi.org/10.1175/1520-0493(2001)129<2570:ACSOTI>2.0.CO;2.

Haynes, P., and M. McIntyre, 1987a: On the representation of Rossby wave critical layers and wave breaking in zonally truncated models. *J. Atmos. Sci.*, **44**, 2359–2382, https://doi.org/10.1175/1520-0469(1987)044<2359:OTRORW>2.0.CO;2.

——, and ——, 1987b: On the evolution of vorticity and potential vorticity in the presence of diabatic heating and frictional or other forces. *J. Atmos. Sci.*, **44**, 828–841, https://doi.org/10.1175/1520-0469(1987)044<0828:OTEOVA>2.0.CO;2.

Hitchman, M., and A. Huesmann, 2007: A seasonal climatology of Rossby wave breaking in the 320–2000-K layer. *J. Atmos. Sci.*, **64**, 1922–1940, https://doi.org/10.1175/JAS3927.1.

Kiladis, G. N., 1998: Observations of Rossby waves linked to convection over the eastern tropical Pacific. *J. Atmos. Sci.*, **55**, 321–339, https://doi.org/10.1175/1520-0469(1998)055<0321:OORWLT>2.0.CO;2.

Knippertz, P., and J. E. Martin, 2005: Tropical plumes and extreme precipitation in subtropical and tropical West Africa. *Quart. J. Roy. Meteor. Soc.*, **131**, 2337–2365, https://doi.org/10.1256/qj.04.148.

Lapeyre, G., and I. M. Held, 2004: The role of moisture in the dynamics and energetics of turbulent baroclinic eddies. *J. Atmos. Sci.*, **61**, 1693–1710, https://doi.org/10.1175/1520-0469(2004)061<1693:TROMIT>2.0.CO;2.

Leroux, M., M. Plu, and F. Roux, 2016: On the sensitivity of tropical cyclone intensification under upper-level trough forcing. *Mon. Wea. Rev.*, **144**, 1179–1202, https://doi.org/10.1175/MWR-D-15-0224.1.

Ling, J., and C. Zhang, 2013: Diabatic heating profiles in recent global reanalyses. *J. Climate*, **26**, 3307–3325, https://doi.org/10.1175/JCLI-D-12-00384.1.

Liu, C., and E. A. Barnes, 2015: Extreme moisture transport into the Arctic linked to Rossby wave breaking. *J. Geophys. Res. Atmos.*, **120**, 3774–3788, https://doi.org/10.1002/2014JD022796.

Lu, J., G. Chen, L. Leung, D. Burrows, Q. Yang, K. Sakaguchi, and S. Hagos, 2015: Toward the dynamical convergence on the jet stream in aquaplanet AGCMs. *J. Climate*, **28**, 6763–6782, https://doi.org/10.1175/JCLI-D-14-00761.1.

Madonna, E., S. Limbach, C. Aebi, H. Joos, H. Wernli, and O. Martius, 2014: On the co-occurrence of warm conveyor belt outflows and PV streamers. *J. Atmos. Sci.*, **71**, 3668–3673, https://doi.org/10.1175/JAS-D-14-0119.1.

Martin, J. E., 2006: *Mid-Latitude Atmospheric Dynamics: A First Course*. John Wiley, 320 pp.

Martius, O., E. Zenklusen, C. Schwierz, and H. C. Davies, 2006: Episodes of Alpine heavy precipitation with an overlying elongated stratospheric intrusion: A climatology. *Int. J. Climatol.*, **26**, 1149–1164, https://doi.org/10.1002/joc.1295.

——, and Coauthors, 2013: The role of upper-level dynamics and surface processes for the Pakistan flood of July 2010. *Quart. J. Roy. Meteor. Soc.*, **139**, 1780–1797, https://doi.org/10.1002/qj.2082.

Masato, G., B. J. Hoskins, and T. Woollings, 2013: Wave-breaking characteristics of Northern Hemisphere winter blocking: A two-dimensional approach. *J. Climate*, **26**, 4535–4549, https://doi.org/10.1175/JCLI-D-12-00240.1.

Massacand, A. C., H. Wernli, and H. C. Davies, 2001: Influence of upstream diabatic heating upon an Alpine event of heavy precipitation. *Mon. Wea. Rev.*, **129**, 2822–2828, https://doi.org/10.1175/1520-0493(2001)129<2822:IOUDHU>2.0.CO;2.

McIntyre, M. E., and T. N. Palmer, 1983: Breaking planetary waves in the stratosphere. *Nature*, **305**, 593–600, https://doi.org/10.1038/305593a0.

Moore, R., and M. Montgomery, 2004: Reexamining the dynamics of short-scale, diabatic Rossby waves and their role in midlatitude moist cyclogenesis. *J. Atmos. Sci.*, **61**, 754–768, https://doi.org/10.1175/1520-0469(2004)061<0754:RTDOSD>2.0.CO;2.

Orlanski, I., 2003: Bifurcation in eddy life cycles: Implications for storm track variability. *J. Atmos. Sci.*, **60**, 993–1023, https://doi.org/10.1175/1520-0469(2003)60<993:BIELCI>2.0.CO;2.

——, and J. P. Sheldon, 1995: Stages in the energetics of baroclinic systems. *Tellus*, **47A**, 605–628, https://doi.org/10.3402/tellusa.v47i5.11553.

Parker, D. J., and A. J. Thorpe, 1995: Conditional convective heating in a baroclinic atmosphere: A model of convective frontogenesis. *J. Atmos. Sci.*, **52**, 1699–1711, https://doi.org/10.1175/1520-0469(1995)052<1699:CCHIAB>2.0.CO;2.

Parker, T. J., G. J. Berry, and M. J. Reeder, 2014: The structure and evolution of heat waves in southeastern Australia. *J. Climate*, **27**, 5768–5785, https://doi.org/10.1175/JCLI-D-13-00740.1.

Payne, A. E., and G. Magnusdottir, 2014: Dynamics of landfalling atmospheric rivers over the North Pacific in 30 years of MERRA reanalysis. *J. Climate*, **27**, 7133–7150, https://doi.org/10.1175/JCLI-D-14-00034.1.

Peters, D., and D. W. Waugh, 1996: Influence of barotropic shear on the poleward advection of upper-tropospheric air. *J. Atmos. Sci.*, **53**, 3013–3031, https://doi.org/10.1175/1520-0469(1996)053<3013:IOBSOT>2.0.CO;2.

Pettersen, S., 1956: *Motion and Motion Systems*. Vol. I, *Weather Analysis and Forecasting*, McGraw-Hill, 428 pp.

Petterssen, S., and S. Smebye, 1971: On the development of extratropical storms. *Quart. J. Roy. Meteor. Soc.*, **97**, 457–482, https://doi.org/10.1002/qj.49709741407.

Polvani, L. M., and J. G. Esler, 2007: Transport and mixing of chemical air masses in idealized baroclinic life cycles. *J. Geophys. Res.*, **112**, D23102, https://doi.org/10.1029/2007JD008555.

Posselt, D., and J. Martin, 2004: The effect of latent heat release on the evolution of a warm occluded thermal structure. *Mon. Wea. Rev.*, **132**, 578–599, https://doi.org/10.1175/1520-0493(2004)132<0578:TEOLHR>2.0.CO;2.

Postel, G. A., and M. H. Hitchman, 1999: A climatology of Rossby wave breaking along the subtropical tropopause. *J. Atmos. Sci.*, **56**, 359–373, https://doi.org/10.1175/1520-0469(1999)056<0359:ACORWB>2.0.CO;2.

Randel, W., and I. Held, 1991: Phase speed spectra of transient eddy fluxes and critical layer absorption. *J. Atmos. Sci.*, **48**, 688–697, https://doi.org/10.1175/1520-0469(1991)048<0688:PSSOTE>2.0.CO;2.

Raymond, D., and H. Jiang, 1990: A theory for long-lived mesoscale convective systems. *J. Atmos. Sci.*, **47**, 3067–3077, https://doi.org/10.1175/1520-0469(1990)047<3067:ATFLLM>2.0.CO;2.

Riemer, M., and S. C. Jones, 2014: Interaction of a tropical cyclone with a high-amplitude, midlatitude wave pattern: Waviness analysis, trough deformation and track bifurcation. *Quart.*

J. Roy. Meteor. Soc., **140**, 1362–1376, https://doi.org/10.1002/qj.2221.

Rivière, G., and I. Orlanski, 2007: Characteristics of the Atlantic storm-track eddy activity and its relation with the North Atlantic Oscillation. *J. Atmos. Sci.*, **64**, 241–266, https://doi.org/10.1175/JAS3850.1.

Rodwell, M., and Coauthors, 2013: Characteristics of occasional poor medium-range weather forecasts for Europe. *Bull. Amer. Meteor. Soc.*, **94**, 1393–1405, https://doi.org/10.1175/BAMS-D-12-00099.1.

Rowe, S. M., and M. H. Hitchman, 2015: On the role of inertial instability in stratosphere–troposphere exchange near midlatitude cyclones. *J. Atmos. Sci.*, **72**, 2131–2151, https://doi.org/10.1175/JAS-D-14-0210.1.

Ryoo, J.-M., Y. Kaspi, D. W. Waugh, G. N. Kiladis, D. E. Waliser, E. J. Fetzer, and J. Kim, 2013: Impact of Rossby wave breaking on U.S. West Coast winter precipitation during ENSO events. *J. Climate*, **26**, 6360–6382, https://doi.org/10.1175/JCLI-D-12-00297.1.

Simmons, A., and B. Hoskins, 1979: The downstream and upstream development of unstable baroclinic waves. *J. Atmos. Sci.*, **36**, 1239–1254, https://doi.org/10.1175/1520-0469(1979)036<1239:TDAUDO>2.0.CO;2.

Sprenger, M., and H. Wernli, 2015: The LAGRANTO Lagrangian analysis tool—version 2.0. *Geosci. Model Dev.*, **8**, 2569–2586, https://doi.org/10.5194/gmd-8-2569-2015.

——, O. Martius, and J. Arnold, 2013: Cold surge episodes over southeastern Brazil—A potential vorticity perspective. *Int. J. Climatol.*, **33**, 2758–2767, https://doi.org/10.1002/joc.3618.

Strong, C., and G. Magnusdottir, 2008: Tropospheric Rossby wave breaking and the NAO/NAM. *J. Atmos. Sci.*, **65**, 2861–2876, https://doi.org/10.1175/2008JAS2632.1.

——, and ——, 2009: The role of tropospheric Rossby wave breaking in the Pacific decadal oscillation. *J. Climate*, **22**, 1819–1833, https://doi.org/10.1175/2008JCLI2593.1.

Sutcliffe, R. C., and A. G. Forsdyke, 1950: The theory and use of upper air thickness patterns in forecasting. *Quart. J. Roy. Meteor. Soc.*, **76**, 189–217, https://doi.org/10.1002/qj.49707632809.

Swenson, E. T., and D. M. Straus, 2017: Rossby wave breaking and transient eddy forcing during Euro-Atlantic circulation regimes. *J. Atmos. Sci.*, **74**, 1735–1755, https://doi.org/10.1175/JAS-D-16-0263.1.

Tamarin, T., and Y. Kaspi, 2016: The poleward motion of extratropical cyclones from a potential vorticity tendency analysis. *J. Atmos. Sci.*, **73**, 1687–1707, https://doi.org/10.1175/JAS-D-15-0168.1.

Teubler, F., and M. Riemer, 2016: Dynamics of Rossby wave packets in a quantitative potential vorticity–potential temperature framework. *J. Atmos. Sci.*, **73**, 1063–1081, https://doi.org/10.1175/JAS-D-15-0162.1.

Thorncroft, C. D., B. J. Hoskins, and M. E. McIntyre, 1993: Two paradigms of baroclinic wave life-cycle behaviour. *Quart. J. Roy. Meteor. Soc.*, **119**, 17–55, https://doi.org/10.1002/qj.49711950903.

Tyrlis, E., and B. J. Hoskins, 2008: The morphology of Northern Hemisphere blocking. *J. Atmos. Sci.*, **65**, 1653–1665, https://doi.org/10.1175/2007JAS2338.1.

Vallis, G. K., Ed., 2017: Planetary waves and zonal asymmetries. *Atmospheric and Oceanic Fluid Mechanics: Fundamentals and Large-Scale Circulation.* Cambridge University Press, 585–626.

Waugh, D. W., and L. M. Polvani, 2000: Climatology of intrusions into the tropical upper troposphere. *Geophys. Res. Lett.*, **27**, 3857–3860, https://doi.org/10.1029/2000GL012250.

Wernli, H., and M. Sprenger, 2007: Identification and ERA-15 climatology of potential vorticity streamers and cutoffs near the extratropical tropopause. *J. Atmos. Sci.*, **64**, 1569–1586, https://doi.org/10.1175/JAS3912.1.

Whitaker, J. S., and C. A. Davis, 1994: Cyclogenesis in a saturated environment. *J. Atmos. Sci.*, **51**, 889–908, https://doi.org/10.1175/1520-0469(1994)051<0889:CIASE>2.0.CO;2.

Wiegand, L., and P. Knippertz, 2014: Equatorward breaking Rossby waves over the North Atlantic and Mediterranean region in the ECMWF operational Ensemble Prediction System. *Quart. J. Roy. Meteor. Soc.*, **140**, 58–71, https://doi.org/10.1002/qj.2112.

Woollings, T., B. Hoskins, M. Blackburn, and P. Berrisford, 2008: A new Rossby wave breaking interpretation of the North Atlantic Oscillation. *J. Atmos. Sci.*, **65**, 609–626, https://doi.org/10.1175/2007JAS2347.1.

Wright, J. S., and S. Fueglistaler, 2013: Large differences in reanalyses of diabatic heating in the tropical upper troposphere and lower stratosphere. *Atmos. Chem. Phys.*, **13**, 9565–9576, https://doi.org/10.5194/acp-13-9565-2013.

Zhang, F., N. Bei, R. Rotunno, C. Snyder, and C. C. Epifanio, 2007: Mesoscale predictability of moist baroclinic waves: Convection-permitting experiments and multistage error growth dynamics. *J. Atmos. Sci.*, **64**, 3579–3594, https://doi.org/10.1175/JAS4028.1.

Zhang, G., Z. Wang, T. J. Dunkerton, M. S. Peng, and G. Magnusdottir, 2016: Extratropical impacts on Atlantic tropical cyclone activity. *J. Atmos. Sci.*, **73**, 1401–1418, https://doi.org/10.1175/JAS-D-15-0154.1.

——, ——, M. Peng, and G. Magnusdottir, 2017: Characteristics and impacts of extratropical Rossby wave breaking during the Atlantic hurricane season. *J. Climate*, **30**, 2363–2379, https://doi.org/10.1175/JCLI-D-16-0425.1.